ORIGINAL PAPER

Geochemistry of Eocene-Early Oligocene low-temperature crustal melts from Greater Himalayan Sequence (Nepal): a nanogranitoid perspective

Omar Bartoli[1] · Antonio Acosta-Vigil[2] · Bernardo Cesare[1] · Laurent Remusat[3] · Adriana Gonzalez-Cano[3] · Markus Wälle[4] · Lucie Tajčmanová[5] · Antonio Langone[6]

Abstract

Despite melt inclusions in migmatites and granulites provide a wealth of information on crustal anatexis in different geological scenarios, a complete compositional study (including trace elements and H_2O) is yet to be made for the Himalayan rocks. In this contribution, we focus on nanogranitoids occurring in peritectic garnet of migmatites from Kali Gandaki valley in central Nepal (Greater Himalayan Sequence, GHS). The microstructural position of the nanogranitoids proves that these melts were produced at 650–720 °C and 1.0–1.1 GPa, during the Eohimalayan prograde metamorphism (41–36 Ma) associated with crustal thickening. Nanogranitoid compositions (mostly granodiorites, tonalites and trondhjemites) resemble those of experimental melts produced during H_2O-present melting of meta-sedimentary rocks. They have variable H_2O concentrations (6.5–14.4 wt%), which are similar to the expected minimum and maximum values for crustal melts produced at the inferred P–T conditions. These compositional signatures suggest that melt formation occurred in the proximity of the H_2O-saturated solidus, in a rock-buffered system. The low-to-very low contents of Zr (3–8 ppm), Th (0.1–1.2 ppm) and LREE (4–11 ppm) along with the weak-to-moderate positive Eu anomalies (Eu/Eu* = 1.2–3.3), the high B concentrations (200–3400 ppm) and the high U/Th ratio (up to 21) point to the lack of equilibration between melt and accessory minerals and are consistent with melting of plagioclase at low temperature. Kali Gandaki nanogranitoids record the beginning of melting in a H_2O-present system that, in other GHS localities, may have produced voluminous crustal melts. We demonstrate that compositional comparison with nanogranitoids may be useful to reconstruct the petrogenesis of Eohimalayan granitoids.

Keywords Nanogranitoids · Greater Himalayan Sequence · Low-T crustal melts · H_2O-present melting

Introduction

The Himalaya mountain belt is the largest active collisional orogen on our planet and is an ideal natural laboratory for investigating orogenic processes (Kohn 2014). This mountain chain has resulted from collision between India and Asia at c. 54–50 Ma (Hodges 2000) or at c. 59 Ma (Hu et al.

✉ Omar Bartoli
omar.bartoli@unipd.it

1 Dipartimento di Geoscienze, Università degli Studi di Padova, Padua, Italy

2 Instituto Andaluz de Ciencias de la Tierra, CSIC-Universidad de Granada, Granada, Spain

3 Muséum National d'Histoire Naturelle, Institut de Minératogie, de Physique des Matériaux et de Cosmochimie,

IMPMC, Sorbonne Université, UMR CNRS 7590, lRD, Paris, France

4 REAIT, CRC and CFI Services (CCCS), Memorial University of Newfoundland, St. John's, Canada

5 Institute of Earth Sciences, Heidelberg University, Heidelberg, Germany

6 Istituto di Geoscienze e Georisorse, C.N.R. University of Pavia, Pavia, Italy

2016). The structural and metamorphic evolution of this orogenic belt is divided into two main phases (Hodges 2000): an Eocene-Late Oligocene Eohimalayan phase during which crustal thickening occurred and most metamorphic rocks reached peak conditions in the kyanite stability field, and an Early Miocene to present Neohimalayan phase characterized by formation of sillimanite-bearing rocks and leucogranites which intruded the higher portions of the Himalayan belt—the so called "Himalayan leucogranites"—whose largest plutons formed at c. 21 Ma (Harrison 2006).

Himalayan leucogranites and the associated Miocene migmatites have been investigated for decades (Weinberg 2016 and references therein). A number of works have established that Miocene anatexis and leucogranite formation occurred by fluid-absent melting of muscovite during decompression (e.g., Inger and Harris 1992; Pognante and Benna 1993; Harris et al. 1995; Harris and Massey 1994; Davidson et al. 1997). Recently, some works have argued that decompression was a consequence rather than a cause of melting (e.g., Rubatto et al. 2013) and the recent review paper by Weinberg (2016) has demonstrated the complexity of Neohimalayan anatexis which records differences in P–T–X_{H2O} conditions, timing and duration across the Himalayas.

Much fewer constraints are available on anatexis during crustal thickening (i.e., the Eohimalayan anatexis), partly because of pervasive Miocene thermal overprint. Where evidence exists, the majority of works have dealt with the age and P–T conditions of high-grade metamorphic processes (e.g. Hodges et al. 1996; Godin et al. 2001; Groppo et al. 2010; Zhang et al. 2010, 2015, 2017; Guilmette et al. 2011; Rubatto et al. 2013; Palin et al. 2014; Wang et al. 2013, 2015; Iaccarino et al. 2017), without shedding light on the composition of crustal melts which, in turn, may provide important, and otherwise impossible to retrieve, information on melting mechanisms (e.g., Acosta-Vigil et al. 2010, 2012a, 2017; Sawyer 2010, Carvalho et al. 2016, 2017, 2019; Weinberg and Hasalová 2015a). For instance, an unusual Ca-rich leucogranite of Late Oligocene age (c. 27.5 Ma) was considered to provide a rare insight into the pre-Miocene melting associated to crustal thickening (Zhang et al. 2004).

In this contribution, we present for the first time the trace element and H_2O contents of melt inclusions (i.e., nanogranitoid inclusions or simply nanogranitoids; Cesare et al. 2015; Bartoli et al. 2013a, 2016a; Ferrero and Angel 2018) from the Himalaya mountain belt. Nanogranitoids come from the Greater Himalayan Sequence—which constitutes the high-grade crystalline core of the orogen—and are present in a microstructural position that clearly proves an Eohimalayan origin for these droplets of crustal melt (Carosi et al. 2015).
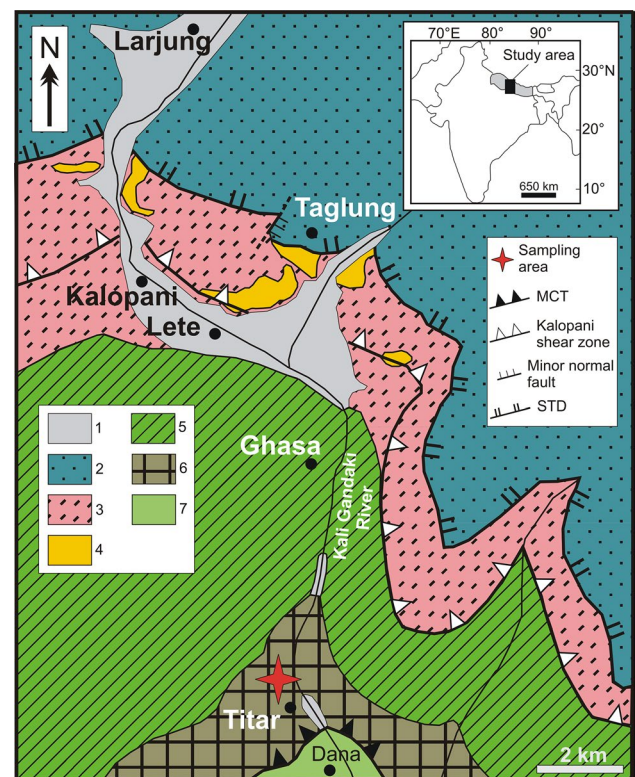

Fig. 1 Geological sketch map of the Kali Gandaki valley (redrawn from Carosi et al. 2015). 1, alluvial debris; 2, Tethyan Sedimentary Sequence (TSS); 3, orthogneiss (GHS); 4, metapelite (GHS); 5, calc-silicate and marble (GHS); 6, kyanite-gneiss (GHS); 7, quartzite (Lesser Himalaya)

Geological background and sampling

From south to north, the Himalayan belt is divided into four tectonic units—Sub-Himalayan molasses, Lesser Himalayan Sequence, Greater Himalayan Sequence (GHS) and Tethyan Himalayan Sequence (THS)—which are separated by important tectonic structures, i.e. Main Boundary Thrust, Main Central Thrust (MCT) and South Tibetan Detachment System (Hodges 2000 and references therein; Fig. 1a). The GHS is a 20–30 km thick sequence of medium-to-high-grade metamorphic rocks and represents the metamorphic core of the Himalaya (Searle and Godin 2003). Several levels of tectono-metamorphic discontinuities were identified within the GHS (Carosi et al. 2018).

The sample under investigation comes from the N–S trending Kali Gandaki valley of central Nepal (Fig. 1b), one of the most classic study areas of the Himalaya (see Carosi et al. 2014 and references therein). Here, GHS reaches a structural thickness of 10–15 km (Godin 2003), shows a NE-dipping prominent high-grade foliation with SW-verging isoclinal folds (Brown and Nazarchuk 1993; Godin 2003; Kellett and Godin 2009; Searle 2010) and can be subdivided
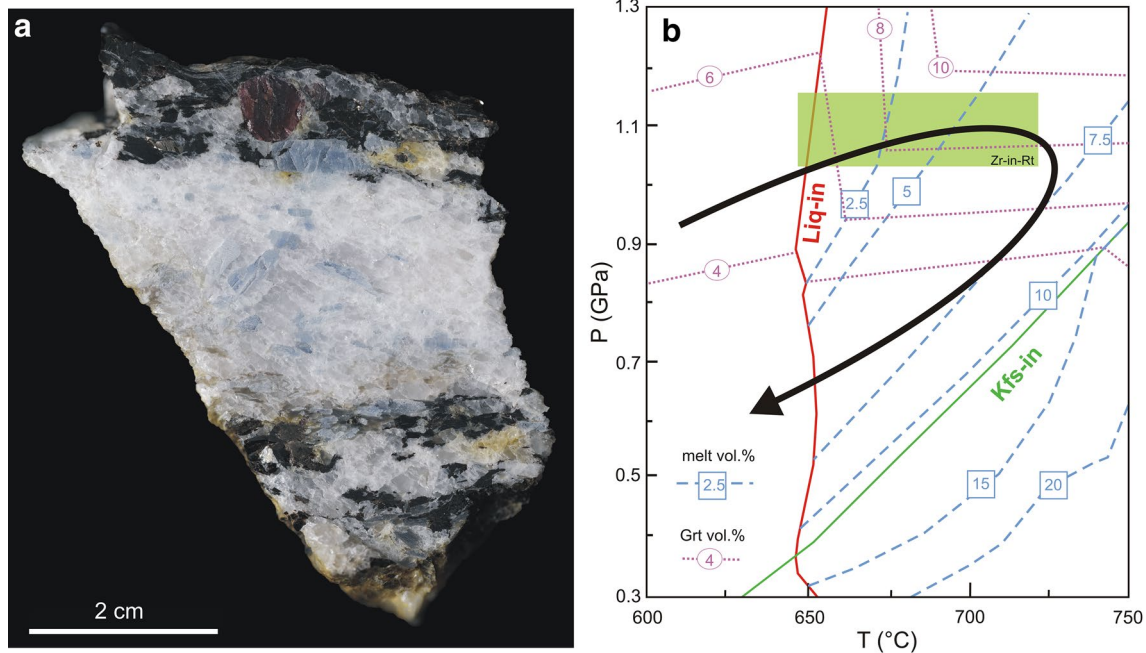
Fig. 2 a Representative hand specimen of the anatectic paragneisses. **b** Phase equilibria modeling and *P–T* path of Ky-bearing gneisses from Kali Gandaki valley (redrawn from Iaccarino et al. 2015). After diverse calculations, the bulk H_2O content was arbitrary fixed at 2 wt%. Too low H_2O amounts stabilize K-feldspar, which is not observed in Kali Gandaki gneisses. Green rectangle: temperature range from the thermometer based on Zr content in rutile (data from Iaccarino et al. 2015)

in three units (Searle and Godin 2003; Searle 2010): the lowest Unit 1 is represented by kyanite-bearing gneisses and migmatites, the Unit 2 consists of clinopyroxene-garnet-amphibole-bearing calcsilicate gneisses, whereas Unit 3 is made of orthogneisses and minor metapelites.

The nanogranitoid-bearing garnet crystal selected for this study has been collected from the debris at the base of an outcrop of kyanite-bearing migmatitic paragneiss (lower part of Unit 1), located close to Titar village (North of Dana village, Fig. 1b). In this outcrop, gneisses have a porphyroblastic texture and contain quartz + plagioclase + biotite + garnet + kyanite + white mica (Fig. 2a). Monazite, xenotime, apatite, zircon, tourmaline, rutile, ilmenite and pyrite are present as accessory minerals. Ilmenite is present in the matrix, whereas rutile occurs only as relict cores in the former mineral and within garnet and kyanite. Microscale shear bands and sigma-type porphyroclasts indicate a top-to-the S sense of shear (additional information in Carosi et al. 2015 and Iaccarino et al. 2015). Tonalitic leucosomes, mainly made of quartz + plagioclase + kyanite, occur parallel to the main foliation defined by biotite and white mica (Fig. 2a). In places, leucosomes form tight to isoclinal folds with axial planes parallel to the main foliation (S_p, Iaccarino et al. 2015). Melanosome mostly contains garnet, biotite, white mica and kyanite. Garnet crystals both in the rock matrix and collected at the base of the outcrop contain similar mineral and melt inclusions and show exactly similar compositional

features (Carosi et al. 2015; Iaccarino et al. 2015), indicating that the dispersed investigated garnet comes from the adjacent Ky-bearing migmatites.

Phase equilibria modeling of migmatitic paragneisses indicates peak conditions of 710–720 °C and 1.0–1.1 GPa, whereas the application of Zr-in-rutile thermometer yielded temperatures of ≈ 650–720 °C (at *P* = 1.1 GPa), interpreted as prograde temperatures (Fig. 2b; Iaccarino et al. 2015). These rocks underwent anatexis with the subsequent formation of leucosomes' close-to-peak conditions, and then decompression and cooling to 650–670 °C and 0.7–0.8 GPa (Iaccarino et al. 2015). The calculated amount of melt generated at peak conditions is ≈ 7.5 vol% (Fig. 2b), approaching the critical threshold for melt interconnection and migration (≈ 7 vol%; Rosenberg and Handy 2005). As a matter of fact, melt accumulation is observed in leucosomes and in dilational structures, whose total volume is far more than the predicted amount of melt at peak conditions (Fig. 2a) (see Iaccarino et al. 2015).

In situ U–Th–Pb geochronology of monazite grains hosted in diverse minerals including melt inclusion-bearing garnet has constrained the timing of nanogranitoids formation at c. 41–36 Ma (Carosi et al. 2015). Iaccarino et al. (2015) performed further in situ dating of monazite from Ky-bearing migmatitic gneisses from the same area and found that monazites included in peritectic garnet, as well as cores of monazite grains in the rock matrix and in

kyanite, are characterized by medium Y contents (Mnz I) and yield ages of c. 43–36 Ma. Conversely, ages of c. 29 Ma are recorded in the mantle of matrix monazite and in the mantle of grains within kyanite (Mnz II). These monazites have low HREE and Y contents. The two populations were interpreted to date the prograde upper-amphibolite facies metamorphism (Mnz I) and "the growth from a melt where garnet was part of the peritectic assemblage" (Mnz II). On the basis of these and previous geochronological constraints, crustal anatexis in the kyanite stability field in Kali Gandaki valley, and in general, in central and eastern Nepal, was ascribed to the underthrusting of the GHS beneath THS following continental collision (Carosi et al. 2015).

Nanogranitoid inclusions

The investigated garnet is 10 mm in diameter and contains hundreds of nanogranitoid inclusions showing a systematic distribution in an annulus located in an intermediate position between core and rim (Fig. 3a, b). Nanogranitoids are 10–20 µm in size, often show an irregular shape and coexist with tiny single mineral inclusions of ilmenite, rutile, apatite, zircon and monazite (Fig. 3c–f). These minerals also appear within melt inclusions (Fig. 3f) and represent accidental trapped phases, as suggested by their relative large size compared with the size of the inclusions, by their low solubility in crustal melts and by the presence of indentations within the inclusion walls (e.g., Cesare and Maineri 1999; Barich et al. 2014). Kyanite is not present as mineral inclusions within the investigated garnet, as already observed for other garnet porphyroblasts occurring in Ky-bearing migmatites from this area (Carosi et al. 2015). Cryptocrystalline aggregates of quartz + plagioclase + muscovite + chlorite ± biotite commonly constitute nanogranitoids (Fig. 3c–f; see also Carosi et al. 2015), suggesting the former presence of a Si- and Al-rich melt. Analysis by EMP of the nanogranitoids that were re-homogenized in the piston cylinder apparatus at 820 °C (see details in Bartoli et al. 2013b) has confirmed the granitoid and peraluminous composition of the trapped melt ($SiO_2 > 65$ wt%, $FeO \approx 2$ to 3 wt%, $CaO \approx 1$ to 4 wt%, $Na_2O \approx 1$ to 4 wt%, $K_2O \approx 0.3$ to 2, $P_2O_5 \approx 0.2$ wt% ASI ≥ 1.3) (see supplementary Table 1).
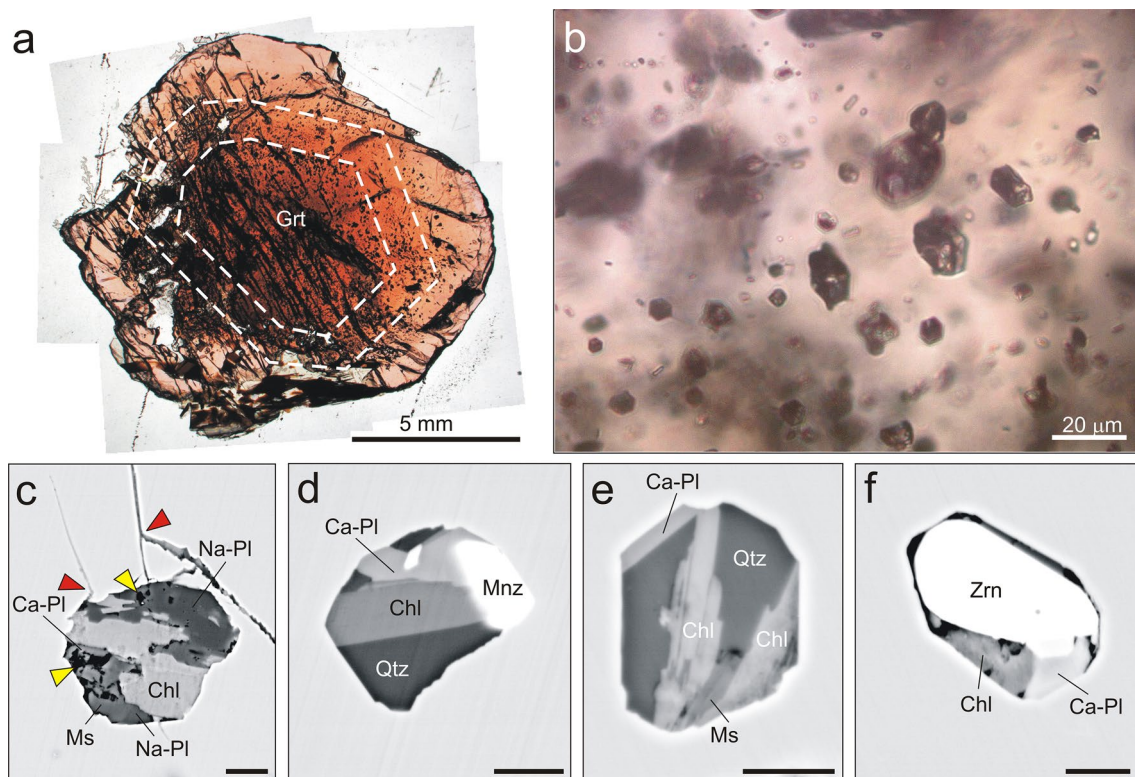

Fig. 3 Melt inclusions in garnet from Kali Gandaki. **a** Plane-polarized photomicrograph of the equatorial section of the investigated garnet. Dashed white lines define the annulus containing nanogranitoid inclusions (redrawn after Cesare et al. 2015). **b** Plane-polarized photomicrograph showing a cluster of polycrystalline inclusions. **c–f** SEM-BSE images of nanogranitoids. Red arrows: decrepitation cracks. Yellow arrows: micro-to-nano-porosity. Scale bar 5 µm

Analytical methods

Trace elements in unexposed and not experimentally re-homogenized inclusions beneath the garnet surface (Table 1) have been analyzed at the Department of Earth Sciences, ETH Zürich by laser ablation inductively coupled plasma mass spectrometry (LA-ICPMS) using a GeoLas system for ablation coupled to an Element XR (Thermo Fisher, Germany). The glass NIST SRM 610 was employed as external standard. The acquired time-resolved signals were processed using the software SILLS (Guillong et al. 2008). Owing to the small size of nanogranitoids, also part of the host garnet has been ablated along with target inclusions. Therefore, the deconvolution of the resulting mixed garnet-glass signal was applied following the procedure of Halter et al. (2002). The Na_2O and FeO contents determined by EMP were used as reference standards for inclusion and garnet, respectively. For elements enriched in the inclusion, the concentrations are accurate within 20–40%. Elements which are strongly compatible in the host garnet (HREE, Y) are normally not detectable in the inclusions due to the dominance of the host signal and were not collected. Gd, V, Zn and Sc show substantially higher contents in the host garnet than in nanogranitoids (Table 1). Therefore, the amount of these elements cannot be reliably estimated in the inclusions. Some inclusions show anomalous very high concentrations of Zr, Th, U, Hf and Nb, suggesting the occurrence of accidental trapped phases (e.g., zircon, monazite, rutile and ilmenite). For these inclusions, contents of Li, B, Rb, Sr, Ba are reported in Table 1 and discussed in the text.

The H_2O measurements of experimentally re-homogenized melt (i.e., glassy) inclusions (Table 2) were performed using the Cameca Nano Secondary Ion Mass Spectrometry 50 (NanoSIMS) installed at Muséum National d'Histoire Naturelle (Paris). Polished experimental capsules with glassy inclusions exposed on the garnet surface and standard glasses were mounted in indium (Aubaud et al. 2007). Inclusions were identified by collecting secondary ion images of Si, Al, K and Fe. For each analysis location, a pre-sputtering step on a 3×3 μm^2 surface area was first done for 2 min with a 360 pA primary Cs^+ beam to remove the gold coating, surface contamination and to reach a steady state sputtering regime (Thomen et al. 2014). Then, a primary beam of 60 pA was used for data acquisition. Data were acquired by rastering a 3×3 μm^2 surface area and collecting ions only from the inner 1×1 μm^2 (using the beam blanking mode) to reduce surface and redeposition contamination. The beam size was, therefore, sufficiently small to analyze solely the melt inclusions. To compensate for charging effects, the electron gun was used while pre-sputtering and during the collecting time. Each analysis is a stack of 200 cycles, a cycle being 1.024 s long. $^{16}OH^-$ (used as a proxy for H_2O),

$^{28}Si^-$, $^{39}K^{16}O^-$ and $^{56}Fe^{16}O^-$ were recorded simultaneously in multicollection mode. We checked that $^{16}OH^-/^{28}Si^-$ ratio was stable during analyses. Secondary ions were collected by electron multipliers with a dead time of 44 ns. Mass resolution was set to 8000, enough to resolve isobaric interference on $^{16}OH^-$. For NanoSIMS calibration, we used granitic glasses with different H_2O contents (for details on calibration procedure and correction curve see Bartoli et al. 2014). Data corrections, using the aforementioned calibration, and error calculations were performed using the R program. Errors combine counting statistics and uncertainty of the calibration curve. However, the errors reported in Table 2 are dominated by the uncertainty of the calibration curve. This uncertainty was calculated by considering a prediction interval, e.g. the range of values that predicts the value of a new observation in the regression analysis of the measurements of the standards that were performed to determine the calibration curve. In the present paper, we considered a 68% prediction interval (that can be considered equivalent to 1σ error). During the session, the vacuum in the analysis chamber remained between 2.5 and 5×10^{-10} Torr.

Results

Melt inclusions show highly variable concentrations of typical incompatible elements such as Li (40–400 ppm), B (200–3400 ppm), Rb (40–400 ppm), Sr (5–100) and Ba (30–900 ppm) (Table 1). The contents of elements typically controlled by the dissolution of accessory minerals are very low (Zr = 3–8 ppm; Th = 0.1–1.2 ppm; LREE = 4–11 ppm). U ranges from 1 to 8 ppm. The Nb/Ta and U/Th ratios are 3–15 and 3–21, respectively. Nanogranitoids also contain appreciable amounts of Sc (3–76 ppm), V (0.4–20 ppm) and Zn (14–92 ppm), though these concentrations might be affected by contamination from the host (see above and Fig. 4a). When compared with the composition of the upper continental crust (Rudnick and Gao 2014), nanogranitoids from Kali Gandaki are enriched in Pb, Li and B, and depleted in Ba, Th, Nb, LREE, MREE, Sr, Zr and Hf (Fig. 4a). On the other hand, Rb, U and Ta show variable degrees of enrichment and depletion. In the chondrite-normalized diagram, melt inclusions show weak-to-moderate positive Eu anomalies (Eu/Eu* = 1.2–3.3) (Fig. 4b).

The H_2O concentrations of the re-homogenized nanogranitoids determined by NanoSIMS span a relatively wide range of values from 6.5 to 10.5 wt%, with one single value up to 14.4 wt% (mean value of 8.9 ± 1.8 wt%; Fig. 5 and Table 2). Melt inclusions were too small to perform replicated analyses within a single inclusion. However, the distribution of H_2O is expected to be quite homogeneous in glassy inclusions obtained from remelting experiments (Bartoli et al. 2014; Acosta-Vigil et al. 2016). H_2O estimated by

**Table 1** LA-ICP-MS analyses (ppm) of melt inclusions and garnet from Kali Gandaki

	KGD_27	KGD_29	KGD_32	KGD_38	KGD_39	KGD_40	KGD_45	KGD_46	KGD_58	KGD_77	KGD_03*	KGD_16*	KGD_08*	KGD_11*	KGD_12*	KGD_34*	KGD_37*	Garnet
Rb	103	59	81	127	60	28	43	46	400	305	b.d.l.	b.d.l.	b.d.l.	b.d.l.	b.d.l.	104	104	1.98
Ba	77	32	42	101	185	44	50	50	606	956	b.d.l.	b.d.l.	b.d.l.	b.d.l.	b.d.l.	85	105	3.48
Pb	60	36	47	88	20	20	37	37	9.6	49	n.c.	n.c.	n.c.	n.c.	n.c.	n.c.	n.c.	0.39
Li	79	58	41	50	329	262	153	153	135	18	424	324	b.d.l.	102	256	58	b.d.l.	7.06
B	1731	847	1068	1005	325	191	244	242	1054	3412	1485	1500	1604	413	1195	1914	1245	12.7
Th	1.2	0.48	0.68	0.48	0.43	0.32	0.20	0.17	0.27	0.12	n.c.	n.c.	n.c.	n.c.	n.c.	n.c.	n.c.	0.02
U	8.5	5.0	6.1	4.8	3.4	1.9	0.56	0.50	1.8	2.5	n.c.	n.c.	n.c.	n.c.	n.c.	n.c.	n.c.	0.10
Nb	b.d.l.	18.28	8.9	1.1	7.3	4.8	8.5	8.3	10.7	5.5	n.c.	n.c.	n.c.	n.c.	n.c.	n.c.	n.c.	1.89
Ta	b.d.l.	1.2	0.86	0.33	2.6	0.31	1.2	1.1	2.1	0.64	b.d.l.	b.d.l.	n.c.	n.c.	n.c.	n.c.	b.d.l.	0.43
La	0.91	0.61	0.70	0.34	0.57	0.59	3.4	3.3	4.0	0.43	n.c.	n.c.	n.c.	n.c.	n.c.	n.c.	n.c.	0.19
Ce	1.7	1.3	0.54	0.53	1.5	1.4	4.0	4.8	3.3	0.88	n.c.	n.c.	n.c.	n.c.	n.c.	n.c.	n.c.	0.40
Sr	84	37	53	59	34	18	29	27	57	76	b.d.l.	b.d.l.	15	4.4	16	106	81	0.72
Nd	b.d.l.	0.41	b.d.l.	b.d.l.	b.d.l.	0.33	2.50	2.48	0.95	0.69	b.d.l.	b.d.l.	n.c.	n.c.	n.c.	n.c.	b.d.l.	0.40
Sm	1.7	0.29	b.d.l.	b.d.l.	b.d.l.	b.d.l.	0.32	0.22	b.d.l.	0.41	n.c.	n.c.	n.c.	n.c.	n.c.	n.c.	n.c.	0.45
Zr	7.3	6.2	8.2	3.2	b.d.l.	3.9	7.5	6.2	4.9	7.8	n.c.	n.c.	n.c.	n.c.	n.c.	n.c.	n.c.	3.66
Hf	b.d.l.	0.34	0.42	b.d.l.	b.d.l.	0.19	0.18	0.29	0.56	0.71	n.c.	n.c.	n.c.	n.c.	n.c.	n.c.	n.c.	0.35
Eu	0.72	0.23	0.67	b.d.l.	b.d.l.	b.d.l.	0.51	0.45	b.d.l.	0.33	b.d.l.	b.d.l.	n.c.	n.c.	n.c.	n.c.	b.d.l.	0.12
Gd	1.9	0.68	1.9	0.96	b.d.l.	0.96	1.3	0.77	b.d.l.	1.3	n.c.	n.c.	n.c.	n.c.	n.c.	n.c.	n.c.	4.31
V	b.d.l.	b.d.l.	b.d.l.	13	20	2.7	0.43	b.d.l.	10.2	b.d.l.	n.c.	n.c.	n.c.	n.c.	n.c.	n.c.	n.c.	44.2
Zn	61	30	92	62	76	14	26	23	54	48	n.c.	n.c.	n.c.	n.c.	n.c.	n.c.	n.c.	77.4
Sc	66	8.0	57	44	76	13	3.1	4.5	16	34	n.c.	n.c.	n.c.	n.c.	n.c.	n.c.	n.c.	87.1
U/Th	7	11	9	10	8	6	3	3	6	21								
Rb/Sr	1.2	1.6	1.5	2.2	1.8	1.6	1.5	1.7	7.0	4.0						1.0	1.3	
Nb/Ta		15.2	10.3	3.2	2.8	15.5	6.8	7.9	5.0	8.5								
Eu/Eu*	1.2	1.6					2.5	3.3		1.4								

b.d.l. below detection limit, *n.c.* not considered

*Nanogranitoid containing accidentally trapped minerals (e.g. zircon, monazite, rutile)

Table 2 H$_2$O concentrations measured in nanogranitoids by NanoSIMS

Sample	Water content (wt%)	1σ error
KGD_1	14.4	0.1
KGD_2	10.5	0.1
KGD_3	10.1	0.1
KGD_4	10.0	0.1
KGD_5	7.7	0.1
KGD_6	8.1	0.1
KGD_7	8.1	0.1
KGD_8	6.9	0.1
KGD_9	9.5	0.1
KGD_10	6.5	0.1
KGD_11	8.8	0.1
KGD_12	8.9	0.1
KGD_13	8.4	0.1
KGD_14	7.3	0.1
KGD_15	8.7	0.1
KGD_16	8.0	0.1
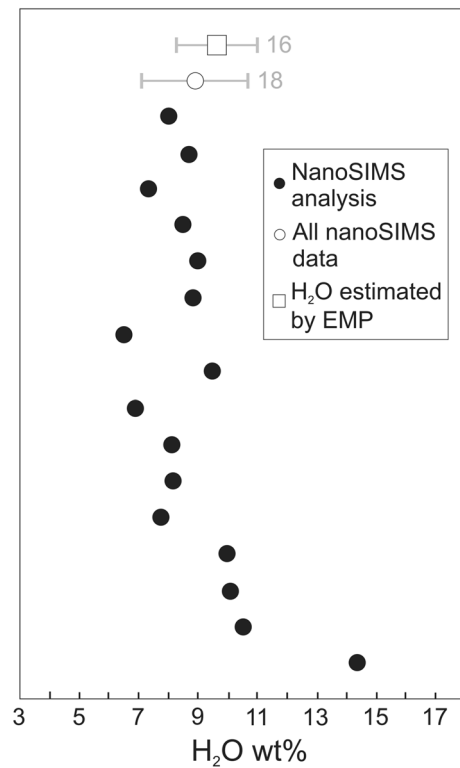
difference of electron microprobe totals from 100% yielded similar mean content (9.6 ± 1.4 wt%) compared to the Nano-SIMS mean data (Fig. 5).

Figure 6 shows zircon and monazite saturation temperatures (T_{Zrn} and T_{Mnz}, respectively) for investigated melt inclusions, calculated following methods proposed by Watson and Harrison (1984), Montel (1993) and Stepanov et al.

Fig. 5 H$_2$O concentrations of nanogranitoid inclusions determined by NanoSIMS. The error associated to these values is smaller than the symbol (see Table 2). White symbols: average contents. The average H$_2$O content estimated by EMP-difference is from Cesare et al. (2015). Horizontal bars are two standard deviations on average values. The number of analyses is indicated next to horizontal bars

Fig. 4 Trace element and REE composition of nanogranitoid inclusions (NG) and host garnet. **a** Values normalized to the average upper continental crust (UCC) composition (data from Rudnick and Gao 2014). **b** REE patterns. Values normalized to the chondrite C1 (Sun and McDonough 1989)
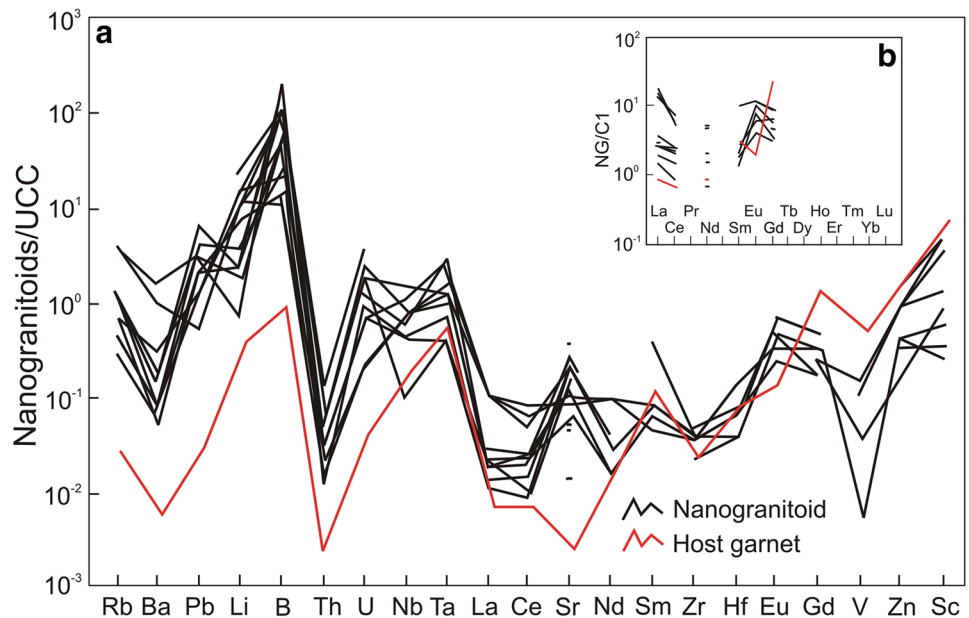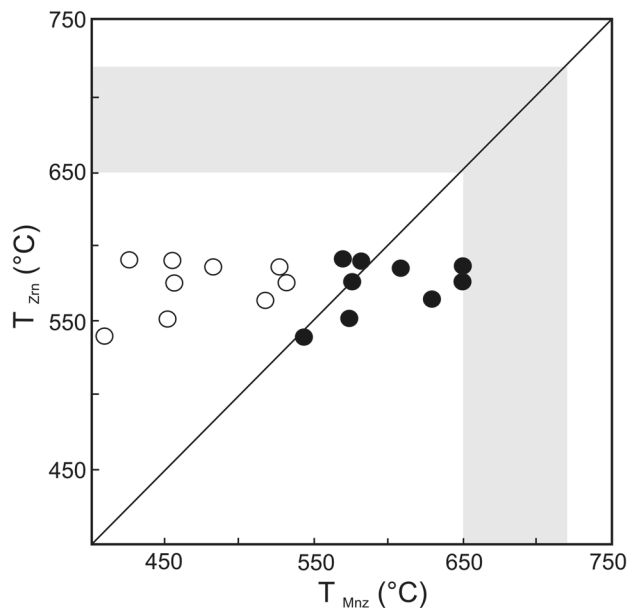
Fig. 6 Monazite and zircon saturation temperatures calculated for the investigated melt inclusions. Black dots: T_{Mnz} calibration of Montel (1993). White dots: T_{Mnz} calibration of Stepanov et al. (2012). T_{Zrn} from Watson and Harrison (1984). Grey field: anatectic temperatures estimated for Kali Gandaki gneisses by Iaccarino et al. (2015)

(2012). We carefully avoided determining T_{Zrn} and T_{Mnz} from nanogranitoids containing trapped mineral inclusions such as zircon or monazite (see above). T_{Zrn} values vary from 541 to 594 °C. The two different calibrations for the T_{Mnz} thermometer provide different temperature ranges such as 544–650 °C (Montel 1993) and 412–533 °C (Stepanov et al. 2012).

Phase equilibria modeling

Migmatites from Kali Gandaki valley have been already investigated by means of phase equilibria modeling (Fig. 2b; Iaccarino et al. 2015). In this contribution, this approach was instead applied considering the average bulk composition of remelted nanogranitoids to compare the predicted subsolidus mineral assemblages with those observed within the inclusions. The average H_2O content used was that estimated by difference from the EMP data, which is consistent with the NanoSIMS values (Fig. 5). Calculations were performed in the Na_2O–CaO–K_2O–FeO–MgO–Al_2O_3–SiO_2–H_2O (NCKFMASH) chemical system, using Perple_x software version 6.8.3. Considering the pitfalls and uncertainties related to phase equilibria approach (White et al. 2011; Bartoli et al. 2013c, 2016b; Forshaw et al. 2019), two P–T sections were calculated for the same bulk composition, one using the internally consistent dataset hp04ver (Holland and Powell 2003) and the older activity–composition (a–x) models, and another calculated using dataset hp11ver (Holland and

Powell 2011) and the re-parameterized a–x models. The following a–x relations were selected: for hp11ver: melt, garnet, chlorite, orthopyroxene, muscovite, biotite and cordierite from White et al. (2014), ilmenite from White et al. (2000), plagioclase and K-feldspar from Holland and Powell (2003). For hp04ver: melt from White et al. (2007), garnet, orthopyroxene and chlorite from Holland and Powell (1998), biotite from Tajčmanová et al. (2009), white mica from Coggon and Holland (2002), plagioclase from Newton et al. (1980) and K-feldspar from Thompson and Hovis (1979). An ideal model was used for cordierite and ilmenite. In all calculations, pure phases included quartz, rutile, kyanite, sillimanite, andalusite and aqueous fluid.

The overall topology of the two P–T sections appears somewhat different, but there are no important variations in terms of phase assemblages (Fig. 7). Modeling of the bulk composition for the nanogranitoids investigated shows the appearance of melt at $T > 680$–690 °C (Fig. 7). The subsolidus field is occupied by various mineral assemblages which are mainly characterized by the presence of chlorite, biotite, muscovite, paragonite, garnet, plagioclase and quartz. At < 500 °C and < 0.4 GPa, the predicted Grt-absent stable mineral assemblages are quartz + plagioclase + muscovite + chlorite + biotite and quartz + plagioclase + muscovite + chlorite (Fig. 7). These assemblages resemble those observed in many nanogranitoid inclusions (see above). Some pores observed during SEM analysis (Fig. 3) likely reflect the former presence of volatiles (in particular H_2O) in excess to the amounts used by phyllosilicates, and therefore, exsolved during crystallization of the melt (see Bartoli et al. 2013a), in agreement with free H_2O predicted by the model at subsolidus conditions (Fig. 7). In addition, both models indicate that chlorite is likely to be a phase formed in the subsolidus during cooling, whose origin did not require infiltration of external fluids (i.e., the presence of chlorite in nanogranitoids does not imply that melt inclusions have been modified by late stage fluid alteration). This finding is also consistent with the coexistence of chlorite and unaltered biotite in nanogranitoids from Ivrea Zone (Carvalho et al. 2019).

Discussion

Nanogranitoids may provide useful information on melting mechanisms and conditions (Acosta-Vigil et al. 2010, 2012a, 2017), and they may shed light on processes which shape the final composition of upper crustal melts (Bartoli et al. 2016a). For Kali Gandaki nanogranitoids, the first point to consider is when they have formed. Next, the constraints on melting conditions and mechanisms are considered, investigating even the probable processes responsible for the observed compositional variability. Finally, a comparative
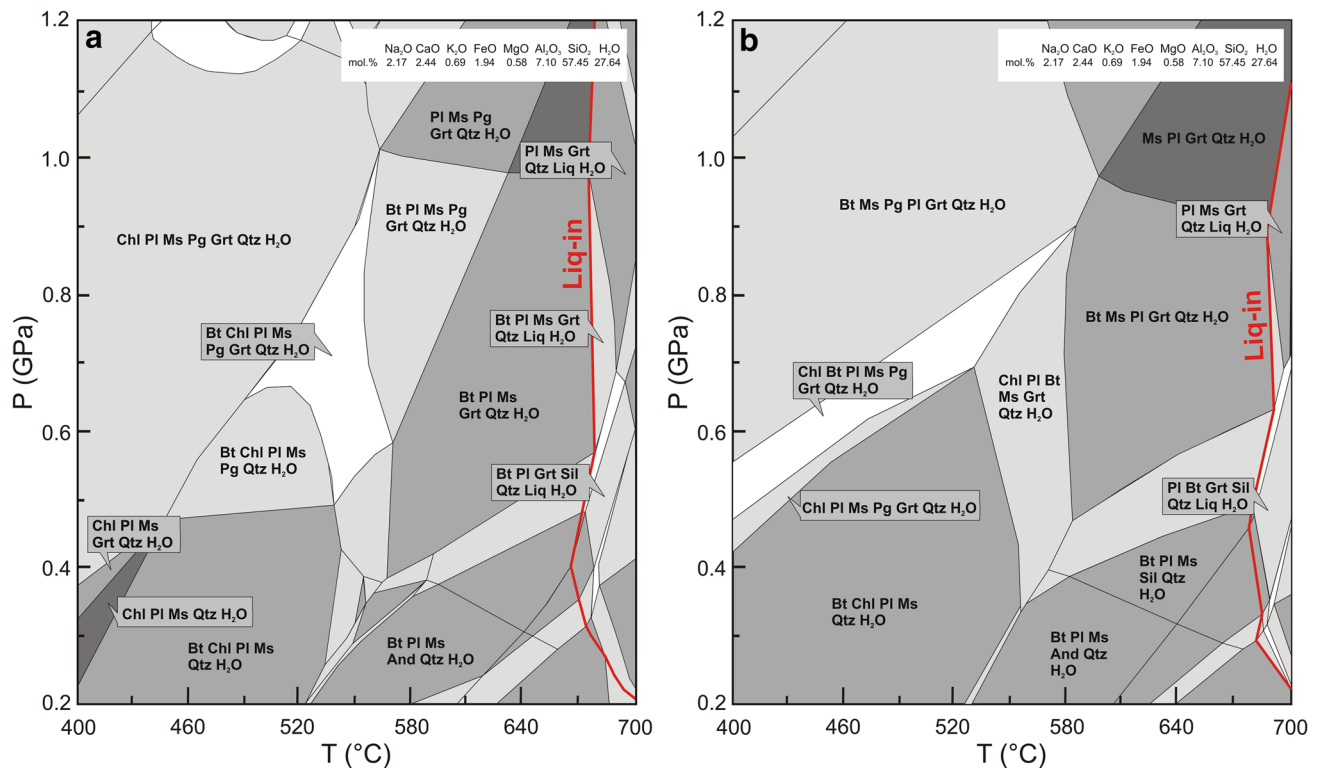
Fig. 7 Comparative *P–T* sections for nanogranitoid inclusions calculated in the NCKFMASH system with two internally consistent datasets: hp04ver for (**a**) and hp11ver for (**b**). The bulk composition (mol%) used for calculation is indicated in the upper right inset and represents the average composition obtained by EMP. The average H_2O content was estimated by EMP difference and is consistent with the NanoSIMS values

study between nanogranitoids and Himalayan granites is presented.

Are the nanogranitoids primary prograde Eohimalayan crustal melts?

Their microstructural distribution, together with the experimental re-homogenization, major and trace element compositions and H_2O contents, and results from phase equilibria modeling (Carosi et al. 2015; Iaccarino et al. 2015; this work) confirm that these polycrystalline inclusions represent former primary melt droplets that have crystallized into a cryptocrystalline aggregate; that is, they are nanogranitoids (Cesare et al. 2015; Bartoli et al. 2016a). Their systematic distribution in an annulus around the garnet core points to a primary origin (Roedder 1979), implying that they were trapped by garnet during growth of the annulus. These microstructural relationships imply that the nanogranitoids represent samples of primary melt present in the partially melted rock at a time when garnet was crystallizing, at or close to the garnet-melt interface. The size of garnet and location of the nanogranitoids imply that the analyzed samples of melt, if they were coeval, were physically separated

from a few tens–hundreds of micrometers to 1 or a few millimeters (Fig. 3a, b).

The annulus of garnet containing melt inclusions certainly formed in the presence of an anatectic melt during incongruent melting (i.e., indicating that this portion has a peritectic origin; Cesare et al. 2015). This is consistent with the increase of garnet mode (5–9 vol%; Iaccarino et al. 2015) predicted by the modeling at the temperature of melting (Fig. 2b). The formation of peritectic garnet at ≤ 700 °C was already documented in Ronda metatexites (S Spain), where it was interpreted as the consequence of a continuous melting reaction that consume biotite (Bartoli et al. 2013c). Also, a geochemical signature typical of muscovite breakdown melting was found in melt inclusions hosted in peritectic garnet from El Hoyazo anatectic enclaves (SE Spain), indicating that this peritectic mineral likely grew (and trapped melt droplets) through melting reactions consuming Fe-bearing muscovite at around 700–750 °C (Acosta-Vigil et al. 2010). Sola et al. (2017) and Schwindinger et al. (2019) demonstrated by means of phase equilibria modeling that small quantities of free H_2O stabilize anhydrous peritectic minerals at lower temperatures. For example, at 1 GPa, the first appearance of garnet is at 760 °C under dry conditions, whereas it occurs at 720 and 680 °C with 1 and 1.5 wt%

H_2O added, respectively (cf. Fig. 7a in Schwindinger et al. 2019). These results are consistent with the formation of peritectic garnet very close to the H_2O-saturated solidus of Ronda metatexites (Bartoli et al. 2013c).

The investigated garnet was collected at the base of a rock wall made of Ky-bearing, partially melted gneiss. Rocks from this outcrop have been intensively studied in the recent years. On the basis of thermodynamic modeling, peritectic garnet likely grew in the presence of a melt phase during white mica breakdown, from 650 to 720 °C, at 1.0–1.1 GPa (Fig. 2b; Iaccarino et al. 2015). In situ U–Th–Pb dating of monazite grains included in melt inclusion-bearing garnets indicates the beginning of anatexis at c. 41–36 Ma (Carosi et al. 2015; Iaccarino et al. 2015). Near peak-pressure melting has been dated at c. 36–28 Ma (Iaccarino et al. 2015). These geochronological constraints are in agreement with the age of c. 35 Ma obtained by U–Pb monazite and zircon dating of a Ky-bearing leucosome collected close to Taglung (Godin et al. 2001), 10–12 km from the Titar village where the investigated nanogranitoids come from.

Considering their primary origin and the geochronological constraints reported above, it is reasonable to interpret that the investigated nanogranitoids reflect primary anatectic melts produced during the Eocene-Early Oligocene (Eohimalayan) prograde metamorphism associated to crustal thickening during the early stages of the India–Asia collision.

Conditions and mechanisms of Eohimalayan anatexis in Kali Gandaki

Most re-homogenized nanogranitoids from Kali Gandaki valley are granodiorites, tonalites and trondhjemites, and minor granites, showing low K_2O (< 2.5 wt%) and high CaO (up to 4 wt%) contents, and moderate–to-very high Na_2O/K_2O ratios (1.1–14.1). In the Qtz–Or–Ab normative diagram, the available major element analyses plot away from the H_2O-saturated haplogranite eutectics, defining an elongated trend parallel to the Qtz-Ab sideline, with large Qtz/feldspars and relatively narrow Or/Ab ratios (Fig. 8). Notably, leucosomes in Kali Gandaki gneisses exhibit a tonalitic composition (Iaccarino et al. 2015), even though this composition could reflect cumulus phenomena which are well documented in leucosomes of migmatites (Brown et al. 2016).

The peculiar major element compositions (see supplementary Table 1) resemble those of experimental melts produced during H_2O-present melting of meta-sedimentary rocks (Fig. 8). For instance, Patiño Douce and Harris (1998) experimentally remelted two GHS schists from the hanging wall of the Main Central Thrust. Melts produced by dehydration melting of mica at > 750 °C (0.6–1.0 GPa) are granitic in compositions ($Na_2O/K_2O = 0.7$–0.9, one value up to 1.4). Instead, near-solidus melts formed at < 750 °C
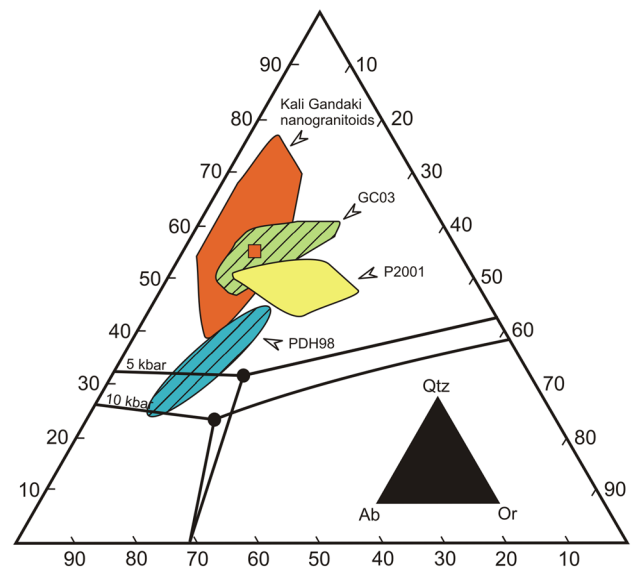

Fig. 8 Qtz–Ab–Or diagram showing the normative compositions of Kali Gandaki nanogranitoids (square represents the average value). Compositions of experimental glasses (PDH98: Patiño Douce and Harris 1998; GC03: García-Casco et al. 2003) and Eohimalayan granites (P2001: Prince et al. 2001) are plotted for comparison

by H_2O-present melting of muscovite correspond to trondhjemites ($Na_2O/K_2O = 1.4$–3.9, one value of 0.9). The $Na_2O/K_2O > 1$ of melt has been ascribed to the decreasing temperature of quartz + plagioclase solidus with increasing H_2O amount (Patiño Douce and Harris 1998; García-Casco et al. 2003). The weak-to-moderate positive Eu anomaly of Kali Gandaki nanogranitoids (Fig. 4b) would support the role of plagioclase in melting reaction (Gao et al. 2017). Therefore, based on the major element compositions of re-homogenized nanogranitoids, the presence of an aqueous fluid phase during the associated anatexis could be proposed, even though it needs more evidence. Indeed, the sole occurrence of trondhjemitic melts is not diagnostic of a H_2O-present scenario, because pressure and source rock composition may play an important role in forming Ab-rich melts (Schwindinger et al. 2019).

The peculiar Na-rich composition of Kali Gandaki nanogranitoids with respect to classic granitic s.s. anatectic melts cannot be the result of melt-garnet interaction during experimental remelting at temperature (820 °C) higher than that of entrapment (650–720 °C), because the host mineral is virtually Na free. Rather, this discrepancy is likely to be related to kinetics (see below).

Re-homogenized nanogranitoids have high H_2O concentrations (6.5–10.5, one value up to 14.4 wt%; Fig. 5). This range approximates the expected minimum and maximum H_2O contents for anatectic melts produced at these P–T conditions (≈ 6.5 to 15 wt%; Holtz et al. 2001). The H_2O content approaching the maximum solubility value (≈ 15

wt% at the pressure of interest of 1.1 GPa) was found in a single nanogranitoid inclusion and it would be consistent with partial melting under fluid-present conditions at the H_2O-saturated solidus. The lower H_2O concentrations may reflect different processes. (1) Weinberg and Hasalová (2015b) argue that in the case of a rock-buffered system (i.e., a system characterized by a high rock/fluid ratio), the H_2O-fluxed melting would produce H_2O-undersaturated melts and that the H_2O contents would range between the minimum and maximum values. (2) Alternatively, different buffering assemblages at the microscale may be responsible for variable melt H_2O content. Bartoli et al. (2014) documented that melt inclusions trapped in different garnet crystals in Ronda migmatites (Spain) showed variable H_2O content and interpreted these heterogeneities as the result of melt formation under conditions of "mosaic equilibrium" affecting the activity of H_2O in the coexisting fluid phase and/or the solid assemblages. This explanation seems to be improbable for the Kali Gandaki sample where the distance among analyzed nanogranitoids is in the order of a few tens–hundreds of µm to a few mm. (3) The loss of H_2O after melt inclusion entrapment and/or during remelting experiments cannot be excluded a priori, considering the presence of cracks in some inclusions (Fig. 3c). However, a systematic loss of H_2O from nanogranitoids during subsolidus retrograde history is expected to result in a larger variability of the melt H_2O contents, with compositions approaching dry values. This is not the case here, where melt H_2O contents do not go below 6.5 wt% (Fig. 5).

One could argue that H_2O loss after the melt inclusion was trapped could partly explain the discrepancy between the trapping temperature and the temperature at which nanogranitoids were experimentally remelted (820 °C, Carosi et al. 2015). In fact, H_2O loss would increase the melting temperature of the nanogranitoid inclusions (cf. Fig. 9 in Bartoli et al. 2013b). However, this discrepancy may be explained without taking into account the loss of H_2O. Indeed, higher remelting temperatures could be needed, because melting kinetics play a fundamental role during reheating experiments. Smaller inclusions usually remelt more rapidly than larger ones (Thomas and Klemm 1997) and nanogranitoids from Kali Gandaki show larger size than melt inclusions for which a run duration of 24 h was tested (Bartoli et al. 2013c and discussion therein). Therefore, a process of H_2O loss affecting the majority of analyzed inclusions does not seem to be supported by convincing evidence.

To summarize, the occurrence of near H_2O-saturated melts would support a H_2O-present melting scenario, confirming the inferences based on major element compositions of nanogranitoids. The observed variation in H_2O content, which is likely to be primary and ranges between the expected minimum and maximum values, would suggest

the existence of a H_2O-present, rock-buffered system during Eohimalayan anatexis. Considering the low melting temperature of Kali Gandaki migmatites together with the low proportion of melt predicted by thermodynamic modeling at the estimated peak *P–T* conditions, these observations are consistent with the beginning of anatexis in these rocks in the proximity of the H_2O-saturated solidus (Fig. 2b).

T_{Zrn} and T_{Mnz} are ≈ 100–250 °C lower than suprasolidus temperatures obtained for migmatites collected in the same area (Fig. 6). T_{Zrn} and T_{Mnz} values are also notably lower than the minimum temperature at which crustal protoliths melt in the presence of an aqueous fluid (≈ 650 °C). Migmatites from Kali Gandaki valley contain abundant grains of zircon and monazite within the matrix as well as inclusions in garnet, kyanite, biotite and quartz (Carosi et al. 2015; Iaccarino et al. 2015). In addition, these accessory minerals are present as accidentally trapped phases within some nanogranitoids (Fig. 3d, f). One, therefore, could assume that melt was in contact with, or attached to zircon and monazite during melting. Because zircon and monazite are expected to break down and dissolve at suprasolidus conditions during prograde metamorphism to maintain saturation of the melt (Yakymchuk and Brown 2014; Yakymchuk 2017), the undersaturated composition of melt inclusions with respect to the accessory minerals would suggest a limited time of interaction between zircon/monazite and anatectic melt. On the other hand, the amount of melt was likely low (around the percolation threshold; Fig. 2) and, therefore, the lack of contact with accessory phases cannot be excluded. In any case, the very low T_{Zrn} and T_{Mnz} values have to be ascribed to the lack of equilibration between melt pockets and accessory minerals present in the rock. A degree of disequilibrium involving accessory minerals and melt inclusions in anatectic rocks has been already documented during the entrapment of low-temperature (< 750 °C) melt droplets in El Hoyazo metapelitic enclaves (Acosta-Vigil et al. 2010). In that case, a much smaller difference of 25–50 °C between calculated and expected temperatures has been reported (see discussion in Acosta-Vigil et al. 2012a).

To date, the most complete dataset of trace element compositions of melt inclusions from metapelitic anatectic rocks is that presented by Acosta-Vigil et al. (2010, 2012a). In residual anatectic enclaves within peraluminous dacites of the Neogene Volcanic Province (NVP) of SE Spain, a systematic evolution of trace element content of anatectic melt (recorded as melt inclusions in several minerals and as matrix glass) is observed. Combining microstructural and geochemical data, these authors interpreted that concentrations in melt of Li, Cs and B decrease, whereas those of Zr, Th, REE, V, Cr, Co, Zn increase with increasing melting temperature, due to the consumption of muscovite (main carrier of Li, B and Cs) at low temperature and biotite (main reservoir of Rb) and accessory phases (LREE, Zr, Hf, U,

Th) at higher temperature (Acosta-Vigil et al. 2010). These authors interpreted the melt inclusions in plagioclase and garnet to represent crustal melts formed by the H_2O-present to H_2O-absent muscovite melting reactions, whereas the matrix glass formed by biotite fluid-absent melting (see also Acosta-Vigil et al. 2017).

The majority of investigated nanogranitoids from Kali Gandaki valley show higher B contents, similar Li concentrations and Rb/Sr ratios, and lower Ba, Ce, Th, Zr, Hf and Rb/B values with respect to NVP melts produced at ≤750 °C (Fig. 9). These compositional features support melting at low temperature (as previously concluded based on peak *P–T* conditions and thermodynamic modeling), and indicate undersaturation of melt with respect to the accessory minerals (see above). Two melt inclusions from the garnet have very high Ba contents (>600 ppm; Fig. 9c). The high B contents (Fig. 9a, b) may point to the presence and dissolution of tourmaline during the melt-producing reaction. Indeed, this mineral is a common accessory phase in Ky-bearing gneisses from this area (Iaccarino et al. 2015). Wolf and London (1997) experimentally demonstrated that at the onset of crustal melting, tourmaline breaks down incongruently to assemblages containing Al-, Fe- and/or Mg-bearing solid phases (i.e., garnet, biotite, sillimanite) and a B-enriched melt. Alternatively, the infiltration of B-rich fluids into the anatectic zone and formation of B-enriched melts cannot be ruled out (Acosta et al. 2001; and references therein) and it would be consistent with a melting scenario characterized by the presence of an aqueous fluid (see above).

Acosta-Vigil et al. (2012a) modeled REE abundance in crustal melts of El Hoyazo considering different scenarios (e.g., disequilibrium melting of feldspars, equilibrium dissolution of accessory phases and equilibrium with major and accessory minerals). Similarly, Prince et al. (2001) calculated REE profiles of crustal melts derived from GHS metapelites assuming that REE abundances are controlled by accessory phase dissolution and by disequilibrium melting of plagioclase. Collectively, these calculations indicate that REE-poor melts with a strong positive Eu anomaly can be due to the disequilibrium melting of feldspars. The dissolution of accessory phases, instead, results in higher REE contents and negative Eu anomalies, whereas similar LREE contents associated with a less sharp positive Eu anomaly are produced by the equilibration with plagioclase and accessory minerals (Fig. 10). The LREE patterns of Kali Gandaki nanogranioids differ significantly from models associated with the dissolution of accessory minerals. Rather, the extremely variable LREE concentrations in melt suggest the lack of equilibration between melt and these minerals. The positive Eu anomalies of Kali Gandaki nanogranioids resemble those of models based on the dissolution of feldspars (light blue and dotted green lines in Fig. 10). However, positive Eu anomalies alone are not diagnostic of equilibrium or

disequilibrium melting of feldspars (see Acosta-Vigil et al. 2012a).

Overall, these results seem to indicate that melt produced at the beginning of anatexis is neither entirely homogeneous nor at equilibrium with at least part of the residue (i.e. accessory minerals). To study the mechanisms of anatexis, Acosta-Vigil et al. (2017) proposed to compare melt inclusion compositions in migmatites and granulites and glass compositions from non-equilibrium kinetics melting experiments. Using this approximation and considering the linear trend displayed by re-homogenized nanogranitoid analyses in the Qtz-Or-Ab normative diagram (Fig. 8), these results from Kali Gandaki indicate that, at the beginning of anatexis, the composition of melt is at least partially controlled by the systematics of diffusion in the melt (see Acosta-Vigil et al. 2006, 2012b, 2017). Lack of melt homogenization and melt-residue equilibration, even for the case of melt fractions separated from tens to hundreds of micrometers to a few mm, can be due to either rapid melting and melt entrapment (because diffusivities of Si and Al in granite melt are rather sluggish, whereas diffusivities of alkalis are extremely high; e.g. Acosta-Vigil et al. 2012b), and/or lack of melt interconnection (given that melt proportions are around the critical melt interconnection threshold; Rosenberg and Handy 2005). Similar conclusions regarding the beginning of the process of anatexis were presented by Acosta-Vigil et al. (2017) in the analysis of the composition of glassy melt inclusions in the El Hoyazo anatectic enclaves (Acosta-Vigil et al. 2007, 2010, 2012a). Analogous inferences regarding, in general, the process of crustal anatexis were also provided by Acosta-Vigil et al. (2017) during the analysis of reported nanogranitoid compositions in granulites from Jubrique (Spain; Acosta-Vigil et al. 2016) and the Orlica-Snieznic dome (Bohemian Massif; Ferrero et al. 2015).

Eohimalayan anatexis and granitoid formation

Kyanite-bearing migmatitic gneisses of the lower GHS in the Kali Gandaki valley underwent low temperature (up to 720 °C) Eocene to Early Oligocene anatexis, with the formation of small amounts of melt (≈7.5 vol%; Fig. 2b) at peak conditions (Carosi et al. 2015; Iaccarino et al. 2015). However, similar rocks, which represent significant portions of the metamorphic core of the Himalayas, experienced higher temperatures and/or higher melting degrees at other localities, between Eocene and Late Oligocene. For example, the Ky-bearing migmatites in the Main Central Thrust Zone (Arun valley, eastern Nepal Himalaya) reached peak conditions at 820 °C and 1.3 GPa, during Early Oligocene (≈31 Ma), producing ≈15 vol% melt (Groppo et al. 2010). In the Kharta Area (Southern Tibet), meta-sedimentary migmatites experienced anatectic conditions of 750–800 °C and 1.4 GPa, at ≈33 Ma (Liu et al. 2007). Phase equilibria
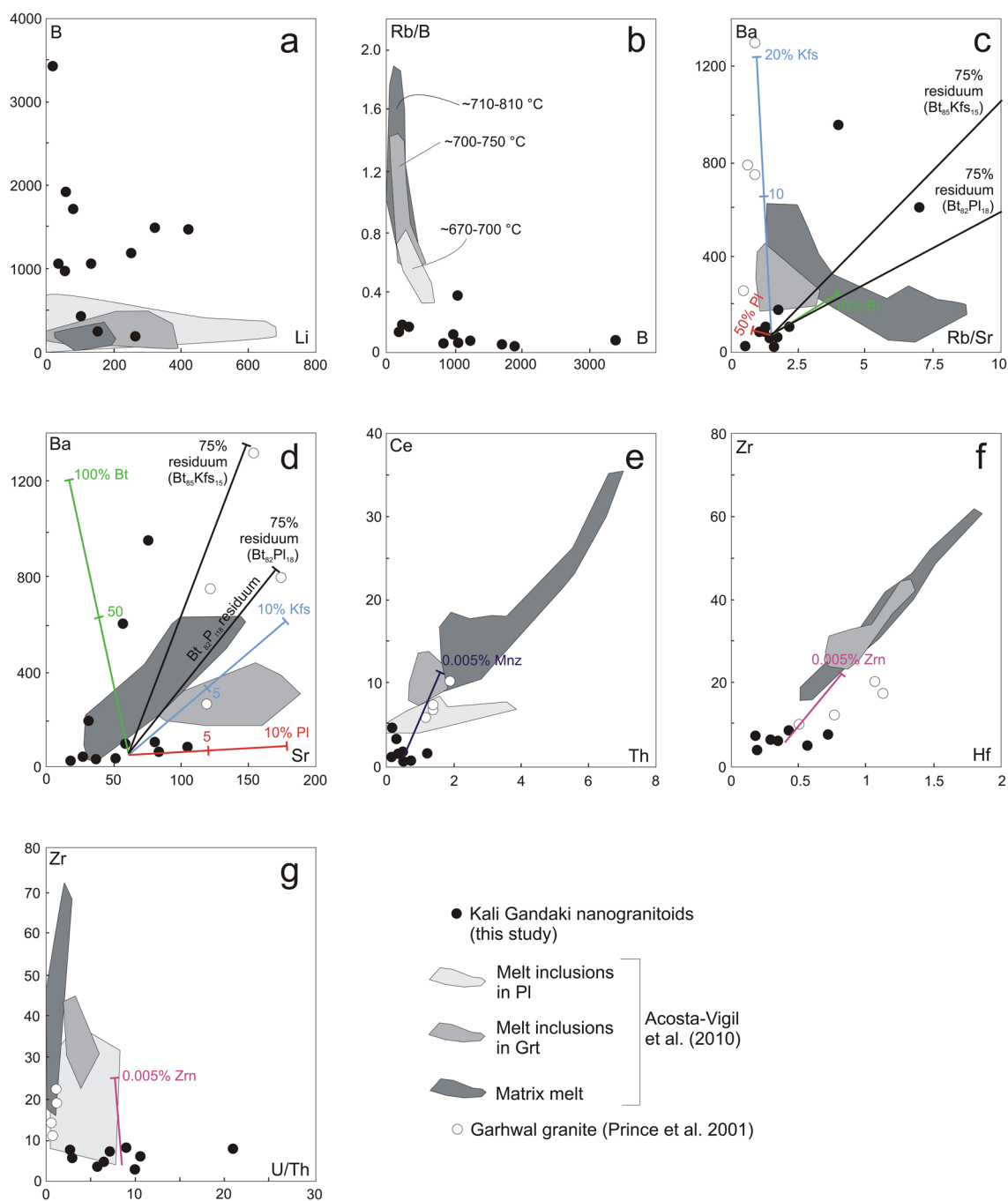
Fig. 9 Comparison among the trace element contents (ppm) of Kali Gandaki nanogranitoids, El Hoyazo melts and Eohimalayan granitoids. Ba and Sr content of melt inclusions in plagioclase were not reported, because these elements are depleted being compatible with respect the host phase; Hf concentrations were not reported for inclusions in plagioclase in the original database (see Acosta-Vigil et al. 2012a). Temperature estimates correspond to zircon and monazite saturation temperatures reported by Acosta-Vigil et al. (2010). Lines track the result of melt–residuum mixing models. Tick marks on the lines reflect increments of the residuum. The average composition of nanogranitoids was considered as representative of the starting melt composition, except for Ba–Rb/Sr and Ba–Sr diagrams where the two Ba-rich melt inclusions were not considered for the average value. This assumption does not change the inferences obtained from the geochemical modeling. Mineral compositions are from Acosta-Vigil et al. (2010). See text for details

modeling demonstrated that Barun gneisses (Eastern Nepal) reached peak conditions of 800–850 °C in the kyanite field, with the formation of 15–20 vol% melt (Groppo et al. 2012).

Melting at the bottom of the GHS (e.g., Barun gneisses) was dated at 33–28 Ma (Carosi et al. 2015 and references therein).

The Namche Barwa Complex (Eastern Himalayan Syntaxis) is considered to represent the NE extension of the GHS (Tian et al. 2016; Guilmette et al. 2011 and references therein). Here, peak conditions of 820 °C and > 1.4 GPa were reported for Ky-bearing anatectic paragneisses by Guilmette et al. (2011). Partial melting is considered to have generated 20–23 vol% total melt. The HP metamorphism was dated at 37–32 Ma (Zhang et al. 2010). Zhang et al. (2015) documented melting of pelitic granulites from the same area at peak conditions of 840–880 °C and 1.3–1.6 GPa; anatexis of these rocks produced up to ≈ 30 vol% melt from c. 40 to 30 Ma. Metagreywackes, instead, reached peak conditions of 820–845 °C and 1.5–1.6 GPa (Tian et al. 2016). Palin et al. (2014) dated the melting at ≈ 700 °C and ≈ 1.0 GPa in the northwestern flank of the Eastern Himalayan Syntaxis between c. 44 and 33 Ma. Leucosomes in Ky-bearing migmatites comprise up to 20% of the outcrop and formed as a result of Kfs-absent, fluid-present melting reactions.

Considering their low melting temperature and degree, Kali Gandaki anatectic gneisses probably did not act as source region of voluminous anatectic melts. However, from the above, it is clear that Ky-bearing migmatites have played an important role during Eohimalayan anatexis. As a matter of fact, melting of meta-sedimentary lithologies from GHS is considered to have contributed to the granitoid magmatism that occurred during crustal thickening at various

temperatures and under various fluid regimes (Prince et al. 2001; Zeng et al. 2009, 2011; Aikman et al. 2012). Therefore, nanogranitoids from Kali Gandaki gneisses, formed in the proximity of the H_2O-saturated solidus, may provide us with the pristine composition of the first batches of melt produced in those lithologies where higher melting degrees have then generated crustal melts whose extraction and emplacement at shallower levels formed the Eohimalayan granitoids.

Granitic to trondhjemitic bodies from the upper GHS of Garhwal Himalaya are considered to be derived from H_2O-present melting of Ky-bearing GHS meta-sedimentary rocks at 650 °C during Eohimalayan prograde metamorphism (39 ± 3 Ma) (Prince et al. 2001). These Eohimalayan granitoids, which differ from the classic Miocene leucogranites, share some key features with the Kali Gandaki melt inclusions, such as Ca- and Na-enrichment (up to 2.0 and 3.9 wt%, respectively), very low melting temperatures and a positive Eu anomaly (Prince et al. 2001). In the haplogranitic Qtz–Ab–Or diagram, the Garhwal rocks plot in the proximity of Kali Gandaki nanogranitoids and experimental glasses produced via H_2O-present melting (Fig. 8). Anatectic gneisses of Kali Gandaki valley may reasonably be considered the analog source rocks of Eohimalayan Garhwal granitoids. Active shear zones in this area could have facilitated the ingress of external fluids, enhancing the amount of melt produced (Prince et al. 2001). Instead, a large supply of external aqueous fluids did not occur in Kali Gandaki area where melting stopped at low degrees.

Granite compositions have been often interpreted in the light of "restite unmixing" model (Chappell et al. 1987), which states that the majority of granites represent mixtures between a minimum or near-minimum temperature melt and the restite (residuum), and that the compositional variability in granites reflects varying degrees of restite unmixing.

The Ba and Sr content of three Garhwal granites can be modeled as the variable mixture of a starting melt (represented by nanogranitoids) and a residuum composed of variable amounts of biotite, plagioclase and K-feldspar (Fig. 9d). One rock needs only the addition of 5 vol% K-feldspar. However, the same mixtures with a biotite-bearing residuum would result in Rb/Sr ratios much higher (≈ 12) than those measured (< 1; Fig. 9c). The very high Ba content and very low Rb/Sr of Garhwal rocks could, instead, be explained by the sole addition of K-feldspar, up to 20 vol% (Fig. 9c). These mismatches clearly indicate that entrapment of residual minerals does not explain the trace element concentrations controlled by major minerals. Although the addition of very tiny amounts of zircon and monazite could explain Ce, Th, U and Zr variability in Garhwal rocks (Fig. 9e, f), this is unlikely. First, the entrainment of phases from the source region is not a selective process (Sawyer 2014). Rather, the inheritance of accessory minerals should be coupled with
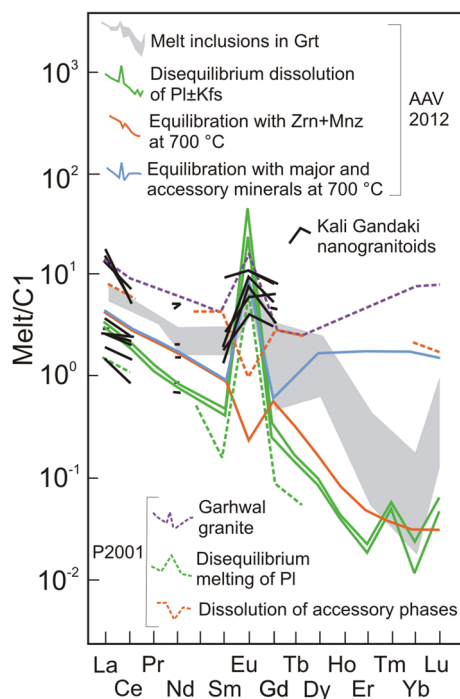

Fig. 10 Comparison of REE abundances of Kali Gandaki nanogranitoids, Garwhal granites and low-temperature anatectic melts modeled by Prince et al. (2001) [P2001] and Acosta-Vigil et al. (2012a) [AAV2012]. See text for details

that of major phases in which they are usually included (micas and feldspars). Again, the mixing with a biotite-, feldspar-bearing residuum is highly improbable (see above). Second, the higher Zr, Th and Ce contents are perfectly consistent with higher degrees of melting compared to those in Kali Gandaki migmatites. Accessory phase dissolution and disequilibrium melting of plagioclase are considered to have shaped the LREE patterns and positive Eu anomaly, respectively, of Garhwal rocks (Fig. 10; Prince et al. 2001). This is mostly in agreement with the diverse La, Ce and Eu contents of Kali Gandaki nanogranitoids whose composition seems to be controlled by the dissolution of plagioclase and lack of equilibrium with accessory minerals (Fig. 10).

Prince et al. (2001) ascribed the very high Ba content of these rocks (> 600 ppm; Fig. 9c) to fluid transport of Ba, which "is a well-documented phenomenon during crustal melting (Weinberg and Searle 1999)". Surprisingly, Ba is highly variable in Kali Gandaki nanogranitoids, formed in a H_2O-present scenario (see above), with the highest contents resembling those observed in some Garhwal rocks (Fig. 9c).

Summarizing, the comparison between nanogranitoids and granites indicates (i) that the restite unmixing process did not shape the composition of Garhwal rocks and that an aqueous fluid was involved in melting process, reinforcing the inferences of Prince et al. (2001), and (ii) that Kali Gandaki melt inclusions are recording the very beginning of melting in a scenario that, in other GHS localities, has produced Eohimalayan granitoids.

Conclusions

Kali Gandaki nanogranitoids occur within peritectic garnet whose formation is ascribed to the Eohimalayan prograde metamorphism at conditions of 650–720 °C and 1.0–1.1 GPa and is dated at c. 41–36 Ma (see Carosi et al. 2015; Iaccarino et al. 2015). During their crystallization, nanogranitoids developed a quartz + plagioclase + muscovite + chlorite ± biotite assemblage. Major element compositions and H_2O contents of re-homogenized nanogranitoids suggest the presence of an aqueous fluid phase during melting, in agreement with the inferred melting conditions. The low Zr, Th and LREE concentrations along with the very low zircon and monazite saturation temperatures indicate disequilibrium between accessory minerals and coexisting melt during anatexis. Investigated nanogranitoids are, therefore, interpreted as incipient melts, which did not have time to fully equilibrate with their source rock.

Kali Gandaki nanogranitoids share some key features with Eohimalayan granitoids from Garhwal Himalaya (i.e.,

major elements, very low melting temperature, Ba enrichment). A comparative study supports previous inferences of Prince et al. (2001): Garhwal rocks likely represent pristine crustal melts formed under H_2O-present conditions, whose composition was not modified by entrainment of residuum. This study confirms the great utility of nanogranitoids to decipher melting mechanisms in the deep crust.

References

Acosta A, Pereira MD, Shaw DM, London D (2001) Contrasting behaviour of B during crustal anatexis. Lithos 56:15–31

Acosta-Vigil A, London D, Morgan GBVI (2006) Experiments on the kinetics of partial melting of a leucogranite at 200 MPa H2O and 690–800 °C: compositional variability of melts during the onset of H2O-saturated crustal anatexis. Contrib Mineral Petrol 151:539–557

Acosta-Vigil A, Cesare B, London D, Morgan GB VI (2007) Microstructures and composition of melt inclusions in a crustal anatectic environment, represented by metapelitic enclaves within El Hoyazo dacites, SE Spain. Chem Geol 235:450–465

Acosta-Vigil A, Buick I, Hermann J, Cesare B, Rubatto D, London D, Morgan GBVI (2010) Mechanisms of crustal anatexis: a geochemical study of partially melted metapelitic enclaves and host dacite, SE Spain. J Petrol 51:785–821

Acosta-Vigil A, Buick I, Cesare B, London D, Morgan GBVI (2012a) The extent of equilibration between melt and residuum during regional anatexis and its implications for differentiation of the continental crust: a study of partially melted metapelitic enclaves. J Petrol 53:1319–1356

Acosta-Vigil A, London D, Morgan GBVI (2012b) Chemical diffusion of major and minor components in granitic liquids: implications for the rates of homogenization of crustal melts. Lithos 153:308–323

Acosta-Vigil A, Barich A, Bartoli O, Garrido C, Cesare B, Remusat L, Poli S, Raepsaet C (2016) The composition of nanogranitoids in migmatites overlying the Ronda peridotites (Betic Cordillera, S Spain): the anatectic history of a polymetamorphic basement. Contrib Mineral Petrol 171:24

Acosta-Vigil A, London D, Morgan VIGB, Cesare B, Buick I, Hermann J, Bartoli O (2017) Primary crustal melt compositions: Insights into the controls, mechanisms and timing of generation from kinetics experiments and melt inclusions. Lithos 286–287:454–479

Aikman AB, Harrison TM, Hermann J (2012) The origin of Eo- and Neo-himalayan granitoids, Eastern Tibet. J Asian Earth Sci 58:143–157

Aubaud C, Withers AC, Hirschmann MM, Guan Y, Leshin LA, Mackwell SJ, Bell DR (2007) Intercalibration of FTIR and

SIMS for hydrogen measurements in glasses and nominally anhydrous minerals. Am Mineral 92:811–828

Barich A, Acosta-Vigil A, Garrido CJ, Cesare B, Tajčmanová L, Bartoli O (2014) Microstructures and petrology of melt inclusions in the anatectic sequence of Jubrique (Betic Cordillera, S Spain): implications for crustal anatexis. Lithos 206–207:303–320

Bartoli O, Cesare B, Poli S, Acosta-Vigil A, Esposito R, Turina A, Bodnar RJ, Angel RJ, Hunter J (2013a) Nanogranite inclusions in migmatitic garnet: behavior during piston cylinder re-melting experiments. Geofluids 13:405–420

Bartoli O, Cesare B, Poli S, Bodnar RJ, Acosta-Vigil A, Frezzotti ML, Meli S (2013b) Recovering the composition of melt and the fluid regime at the onset of crustal anatexis and S-type granite formation. Geology 41:115–118

Bartoli O, Tajčmanová L, Cesare B, Acosta-Vigil A (2013c) Phase equilibria constraints on melting of stromatic migmatites from Ronda (S. Spain): insights on the formation of peritectic garnet. J Metamorph Geol 31:775–789

Bartoli O, Cesare B, Remusat L, Acosta-Vigil A, Poli S (2014) The H_2O content of granite embryos. Earth Planet Sci Lett 395:281–290

Bartoli O, Acosta-Vigil A, Ferrero S, Cesare B (2016a) Granitoid magmas preserved as melt inclusions in high-grade metamorphic rock. Am Mineral 101:1543–1559

Bartoli O, Acosta-Vigil A, Tajčmanová L, Cesare B, Bodnar RJ (2016b) Using nanogranitoids and phase equilibria modeling to unravel anatexis in the crustal footwall of the Ronda peridotites (Betic Cordillera, S Spain). Lithos 256–257:282–299

Brown RL, Nazarchuk JH (1993) Annapurna detachment fault in the Greater Himalaya of Central Nepal. Geol Soc Lond Spec Publ 74:461–473

Brown CR, Yakymchuk C, Brown M, Fanning CM, Korhonen FJ, Piccoli PM, Siddoway CS (2016) From source to sink: petrogenesis of Cretaceous anatectic granites from the Fosdick migmatite-granite complex, West Antarctica. J Petrol 57:1241–1278

Carosi R, Gemignani L, Godin L, Iaccarino S, Larson KP, Montomoli C, Rai SM (2014) A geological journey through the deepest gorge on Earth: the Kali Gandaki valley section, west-central Nepal. J Virtual Explor. https://doi.org/10.3809/Jvirtex.vol.2014.052

Carosi R, Montomoli C, Langone A, Turina A, Cesare B, Iaccarino S, Fascioli L, Visonà D, Ronchi A, Rai SM (2015) Eocene partial melting recorded in peritectic garnets from kyanite-gneiss, Greater Himalayan Sequence, central Nepal. Geol Soc Lond Spec Publ 412:111

Carosi R, Montomoli C, Iaccarino S (2018) 20 years of geological mapping of the metamorphic core across Central and Eastern Himalayas. Earth Sci Rev 177:124–138

Carvalho BB, Sawyer EW, Janasi VA (2016) Crustal reworking in a shear zone: transformation of metagranite to migmatite. J Metamorph Geol 34:237–264

Carvalho BB, Sawyer EW, Janasi VA (2017) Enhancing maficity of granitic magma during anatexis: entrainment of infertile mafic lithologies. J Petrol 58:1333–1362

Carvalho BB, Bartoli O, Ferri F, Cesare B, Ferrero F, Remusat L, Capizzi L, Poli S (2019) Anatexis and fluid regime of the deep continental crust: new clues from melt and fluid inclusions in metapelitic migmatites from Ivrea Zone (NW Italy). J Metamorph Geol 37:951–975

Cesare B, Maineri C (1999) Fluid-present anatexis of metapelites at El Joyazo (SE Spain): constraints from Raman spectroscopy of graphite. Contrib Mineral Petrol 135:41–52

Cesare B, Acosta-Vigil A, Bartoli O, Ferrero S (2015) What can we learn from melt inclusions in migmatites and granulites? Lithos 239:186–216

Chappell BW, White AJR, Wyborn D (1987) The importance of residual source material (Restite) in granite petrogenesis. J Petrol 28:1111–1138

Coggon R, Holland TJB (2002) Mixing properties of phengitic micas and revised garnet–phengite thermobarometers. J Metamorph Geol 20:683–696

Davidson C, Grujic DE, Hollister LS, Schmid SM (1997) Metamorphic reactions related to decompression and synkinematic intrusion of leucogranite, High Himalayan Crystallines, Bhutan. J Metamorph Geol 15:593–612

Ferrero S, Angel R (2018) Micropetrology: Are inclusions grains of truth? J Petrol 59:1671–1700

Ferrero S, Wunder B, Walczak K, O'Brien PJ, Ziemann MA (2015) Preserved near ultrahigh-pressure melt from continental crust subducted to mantle depths. Geology 43:447–450

Forshaw JB, Waters DJ, Pattison DRM, Palin RM, Gopon PA (2019) Comparison of observed and thermodynamically predicted phase equilibria and mineral compositions in mafic granulites. J Metamorph Geol 37:153–179

Gao L-E, Zeng L, Asimow PD (2017) Contrasting geochemical signatures of fluid-absent versus fluid-fluxed melting of muscovite in metasedimentary sources: the Himalayan leucogranites. Geology 45:39–42

García-Casco A, Haissen F, Castro A, El-Hmidi H, Torres-Roldán RL, Millán G (2003) Synthesis of staurolite in melting experiments of a natural metapelite: consequences for the phase relations in low-temperature pelitic migmatites. J Petrol 44:1727–1757

Godin L (2003) Structural evolution of the Tethyan sedimentary sequence in the Annapurna area, central Nepal Himalaya. J Asian Earth Sci 22:307–328

Godin L, Parish RR, Brown L, Hodges KV (2001) Crustal thickening leading to exhumation of the Himalayan Metamorphic core of central Nepal: insight from U-Pb geochronology and 40Ar/39Ar thermochronology. Tectonics 20:729–747

Groppo C, Rubatto D, Rolfo F, Lombardo B (2010) Early Oligocene partial melting in Main Central Thrust Zone (Arun valley, eastern Nepal Himalaya). Lithos 118:287–301

Groppo C, Rolfo F, Indares A (2012) Partial melting in the Higher Himalayan Crystallines of Eastern Nepal: the effect of decompression and implications for the 'Channel Flow' model. J Petrol 53:1057–1088

Guillong M, Meier DL, Allan MM, Heinrich CA, Yardley BWD (2008) SILLS: a MATLAB-based program for the reduction of laser ablation ICP-MS data of homogeneous materials and inclusions. Mineralogical Association of Canada Short Course 40, Vancouver, pp 328–333

Guilmette C, Indares A, Hébert R (2011) High-pressure anatectic paragneisses from the Namche Barwa, Eastern Himalayan Syntaxis: textural evidence for partial melting, phase equilibria modeling and tectonic implications. Lithos 124:66–81

Halter WE, Pettke T, Heinrich CA, Rothen-Rutishauser B (2002) Major to trace element analysis of melt inclusions by laser-ablation ICP–MS: methods of quantification. Chem Geol 183:63–86

Harris N, Massey J (1994) Decompression and anatexis of Himalayan metapelites. Tectonics 13:1537–1546

Harris N, Ayres M, Massey J (1995) Geochemistry of granitic melts produced during the incongruent melting of muscovite: implication for the extraction of Himalayan leucogranite magmas: J Geoph Res 100:15767–15777

Harrison TM (2006) Did the Himalayan crystallines extrude partially molten from beneath the Tibetan Plateau? In: Law RD, Searle MP, Godin L (eds) Geological constraints on channel flow and ductile extrusion as an important orogenic process—Himalaya-Tibetan Plateau, vol 268. Geological Society, London, Special Publication, London, pp 237–254

Hodges KV (2000) Tectonics of the Himalaya and southern Tibet from two perspectives. Geol Soc Am Bull 112:324–350

Hodges KV, Parrish RR, Searle MP (1996) Tectonic evolution of the central Annapurna Range, Nepalese Himalayas. Tectonics 15:1264–1291

Holland TJB, Powell R (1998) An internally consistent thermodynamic data set for phases of petrological interest. J Metamorph Geol 16:309–343

Holland TJB, Powell R (2003) Activity-composition relations for phases in petrological calculations: an asymmetric multicomponent formulation. Contrib Mineral Petrol 145:492–501

Holland TJB, Powell R (2011) An improved and extended internally consistent thermodynamic dataset for phases of petrological interest, involving a new equation of state for solids. J Metamorph Geol 29(3):333–383

Holtz F, Johannes W, Tamic N, Behrens H (2001) Maximum and minimum water contents of granitic melts generated in the crust: a reevaluation and implications. Lithos 56:1–14

Hu X, Garzanti E, Wang J, Huang W, An W, Webb A (2016) The timing of India-Asia collision onset—facts, theories, controversies. Earth Sci Rev 160:264–299

Iaccarino S, Montomoli C, Carosi R, Massonne H-J, Langone A, Visonà D (2015) Pressure–temperature–time–deformation path of kyanite-bearing migmatitic paragneiss in the Kali Gandaki valley (Central Nepal): investigation of Late Eocene-Early Oligocene melting processes. Lithos 231:103–121

Iaccarino S, Montomoli C, Carosi R, Massonne H-J, Langone A, Visonà D (2017) Geology and tectono-metamorphic evolution of the Himalayan metamorphic core: insights from the Mugu Karnali transect, Western Nepal (Central Himalaya). J Metamorph Geol 35:301–325

Inger S, Harris NBW (1992) Tectonothermal evolution of the High Himalayan crystalline sequence, Langtang Valley, northern Nepal. J Metamorph Geol 10:439–452

Kellett DA, Godin L (2009) Pre-Miocene deformation of the Himalayan superstructure, Hidden valley, central Nepal. J Geol Soc Lond 166:261–275

Kohn MJ (2014) Himalayan metamorphism and its tectonic implications. Annu Rev Earth Planet Sci 42:381–419

Liu Y, Siebel W, Massonne H-J, Xiao X (2007) Geochronological and petrological constraints for the tectonic evolution of the central Greater Himalayan Sequence in the Kharta area, southern Tibet. J Geol 115:215–230

Montel JM (1993) A model for monazite/melt equilibrium and applications to the generation of granitic magmas. Chem Geol 110:127–146

Newton RC, Charlu TV, Kleppa OJ (1980) Thermochemistry of high structural state plagioclases. Geochim Cosmochim Acta 44:933–941

Palin RM, Searle MP, St-Onge MR, Waters DJ, Roberts NMW, Horstwood MSA, Parrish RR, Weller OM, Chen S, Yang J (2014) Monazite geochronology and petrology of kyanite- and sillimanite-grade migmatites from the northwestern flank of the eastern Himalayan syntaxis. Gondwana Res 26:323–347

Patiño Douce AE, Harris N (1998) Experimental constraints on Himalayan anatexis. J Petrol 39:689–710

Pognante U, Benna P (1993) Metamorphic zonation, migmatization and leucogranites along the Everest transect of Eastern Nepal and Tibet: record of an exhumation history. Geol Soc Lond Spec Publ 74:323–340

Prince C, Harris N, Vance D (2001) Fluid-enhanced melting during prograde metamorphism. J Geol Soc 158:233–242

Roedder E (1979) Fluid inclusions as samples of ore fluids. In: Barnes HL (ed) Geochemistry of hydrothermal ore deposits, 2nd edn. Wiley, New York, pp 684–737

Rosenberg CL, Handy MR (2005) Experimental deformation of partially melted granite revisited: implications for the continental crust. J Metamorph Geol 23:19–28

Rubatto D, Chakraborty S, Dasgupta S (2013) Timescales of crustal melting in the Higher Himalayan crystallines (Sikkim, Eastern Himalaya) inferred from trace element-constrained monazite and zircon chronology. Contrib Mineral Petrol 165:349–372

Rudnick RL, Gao S (2014) Composition of the continental crust. In: Rudnick RL (ed) Treatise on geochemistry, 2nd edn., pp 1–51

Sawyer EW (2010) Migmatites formed by water-fluxed partial melting of a leucogranodiorite protolith: microstructures in the residual rocks and source of the fluid. Lithos 116:273–286

Sawyer EW (2014) The inception and growth of leucosomes: microstructure at the start of melt segregation in migmatites. J Metamorph Geol 32:695–712

Schwindinger M, Weinberg RF, Clos F (2019) Wet or dry? The difficulty of identifying the presence of water during crustal melting. J Metamorph Geol 37:339–358

Searle MP (2010) Low-angle normal faults in the compressional Himalayan orogen; evidence from the Annapurna-Dhaulagiri Himalaya, Nepal. Geosphere 6:296–315

Searle MP, Godin L (2003) The South Tibetan Detachment System and the Manaslu Leucogranite: a structural reinterpretation and restoration of the Annapurna-Manaslu Himalaya, Nepal. J Geol 111:505–523

Sola AM, Hasalová P, Weinberg RF, Suzaño NO, Becchio RA, Hongn FD, Botelho N (2017) Low-P melting of metapelitic rocks and the role of H2O: insights from phase equilibria modeling. J Metamorph Geol 35:1131–1159

Stepanov AS, Hermann J, Rubatto D, Rapp RP (2012) Experimental study of monazite/melt partitioning with implications for the REE, Th and U geochemistry of crustal rocks. Chem Geol 300–301:200–220

Sun SS, McDonough WF (1989) Chemical and isotopic systematics of oceanic basalts: implications for mantle composition and processes. In: Sanders AD, Norry MJ (eds) Magmatism in the ocean basins, vol 42. Geological Society, London, Special Publications, London, pp 313–345

Tajčmanová L, Conolly JAD, Cesare B (2009) A thermodynamic-model for titanium and ferric iron solution in biotite. J Metamorph Geol 27:153–165

Thomas R, Klemm W (1997) Microthermometric study of silicate melt inclusions in Variscan granites from SE Germany: volatile contents and entrapment conditions. J Metamorph Geol 38:1753–1765

Thomen A, Robert F, Remusat L (2014) Determination of the nitrogen abundance in organic materials by NanoSIMS quantitative imaging. J Anal At Spectrom 29:512–519

Thompson JB, Hovis GL (1979) Entropy of mixing in sanidine. Am Mineral 64:57–65

Tian Z, Zhang Z, Dong X (2016) Metamorphism of high-P metagreywacke from the Eastern Himalayan syntaxis: phase equilibria and P–T path. J Metamorph Geol 34:697–718

Wang JM, Zhang JJ, Wang XX (2013) Structural kinematics, metamorphic P–T profiles and zircon geochronology across the Greater Himalayan Crystalline Complex in south–central Tibet: implication for a revised channel flow. J Metamorph Geol 31:607–628

Wang JM, Rubatto D, Zhang JJ (2015) Timing of partial melting and cooling across the Greater Himalayan Crystalline Complex (Nyalam, Central Himalaya): in-sequence Thrusting and its implications. J Petrol 56(9):1677–1702

Watson EB, Harrison TM (1984) Accessory minerals and the geochemical evolution of crustal magmatic systems: a summary and prospectus of experimental approaches. Phys Earth Planet Inter 35:19–30

Weinberg (2016) Geology and tectono-metamorphic evolution of the Himalayan metamorphic core: insights from the Mugu Karnali transect, Western Nepal (Central Himalaya). J Metamorph Geol 35:301–325

Weinberg R, Hasalová P (2015a) Water-fluxed melting of the continental crust: a review. Lithos 212–215:158–188

Weinberg R, Hasalová P (2015b) Reply to comment by JD Clemens and G. Stevens on "Water-fluxed melting of the continental crust: a review". Lithos 234:102–103

Weinberg R, Searle MP (1999) Volatile-assisted intrusion and autometasomatism of leucogranites in the Khumbu Himalaya, Nepal. J Geol 107:27–48

White RW, Powell R, Holland TJB, Worley BA (2000) The effect of TiO_2 and Fe_2O_3 on metapelitic assemblages at greenschist and amphibolite facies conditions: mineral equilibria calculations in the system $K_2O–FeO–MgO–Al_2O_3–SiO_2–H_2O–TiO_2–Fe_2O_3$. J Metamorph Geol 18:497–511

White RW, Powell R, Holland TJB (2007) Progress relating to calculation of partial melting equilibria for metapelites. J Metamorph Geol 25:511–527

White RW, Stevens G, Johnson TE (2011) Is the crucible reproducible? Reconciling melting experiments with thermodynamic calculations. Elements 7:241–246

White RW, Powell R, Holland TJB, Johnson TE, Green ECR (2014) New mineral activity–composition relations for thermodynamic calculations in metapelitic systems. J Metamorph Geol 32:261–286

Wolf MB, London D (1997) Boron in granitic magmas: stability of tourmaline in equilibrium with biotite and cordierite. Contrib Mineral Petrol 130:12–30

Yakymchuk C (2017) Behaviour of apatite during partial melting of metapelites and consequences for prograde suprasolidus monazite growth. Lithos 274–275:412–426

Yakymchuk C, Brown M (2014) Behaviour of zircon and monazite during crustal melting. J Geol Soc 171:465–479

Zeng LS, Liu J, Gao LE, Xie KJ, Wen L (2009) Early Oligocene crustal anatexis in the Yardoi gneiss dome, southern Tibet and geological implications. Chin Sci Bull 54:104–112

Zeng LS, Gao LE, Xie KJ, Liu-Zeng J (2011) Mid-Eocene high Sr/Y granites in the Northern Himalayan Gneiss Domes: melting thickened lower continental crust. Earth Planet Sci Lett 303:251–266

Zhang H, Harris N, Parrish R, Kelley S, Zhang L, Rogers N, Argles T, King J (2004) Causes and consequences of protracted melting of the mid-crust exposed in the North Himalayan antiform. Earth Planet Sci Lett 228:195–212

Zhang ZM, Zhao GC, Santosh M, Wang JL, Dong X, Liou JG (2010) Two stages of granulite facies metamorphism in the eastern Himalayan syntaxis, south Tibet: petrology, zircon geochronology and implications for the subduction of Neo-Tethys and the Indian continent beneath Asia. J Metamorph Geol 28:719–733

Zhang Z, Xiang H, Dong X, Ding H, He Z (2015) Long-lived high-temperature granulite-facies metamorphism in the Eastern Himalayan orogen, south Tibet. Lithos 212–215:1–15

Zhang Z, Xiang H, Dong X, Li W, Ding H, Gou Z, Tian Z (2017) Oligocene HP metamorphism and anatexis of the Higher Himalayan Crystalline Sequence in Yadong region, east-central Himalaya. Gondwana Res 41:173–187